An assessment of the surface longwave direct radiative effect of airborne dust in Zhangye, China, during the Asian Monsoon Years field experiment (2008)

Richard A. Hansell,[1,2] Si-Chee Tsay,[2] N. Christina Hsu,[2] Qiang Ji,[1,2] Shaun W. Bell,[2,3] Brent N. Holben,[2] Ellsworth J. Welton,[2] Ted L. Roush,[4] W. Zhang,[5] J. Huang,[5] Zhanqing Li,[1,6] and H. Chen[7]

[1] In April–June 2008, NASA Goddard's ground-based mobile laboratories (SMART-COMMIT) were deployed to Zhangye China (39.0°N; 101°W) to support the Asian Monsoon Years field experiment and the East Asian Study of Tropospheric Aerosols and Impact on Regional Climate. One of the primary objectives at Zhangye, a semi-arid region located between the Taklimakan and Gobi Deserts, was to capture and characterize dust aerosols near the source and to quantify their direct radiative effects (DRE). A regional dust optical model was constructed by combining previously measured soil mineralogy data at Zhangye with COMMIT's particle microphysical measurements. During a 2-week period of heightened dust activity, retrieved longwave (LW) aerosol optical thickness (τ) from SMART's Atmospheric Emitted Radiance Interferometer was used in the Fu-Liou radiative transfer model to derive LW instantaneous DRE (DRE_{LW}) at the surface, top of atmosphere, and heating rate profiles for cloud-free conditions. Conservatively, surface instantaneous DRE_{LW} and LW forcing efficiency range from about 2–20 Wm^{-2} and 31–35 $Wm^{-2}\tau^{-1}$ ($0 \leq \tau \leq 0.83$), respectively. The significance of DRE_{LW} relative to its shortwave counterpart was estimated to be between 51 and 58%, but of opposite sign, partly compensating shortwave surface cooling. Compared to Saharan dust observed during the NAMMA-2006 field experiment at Cape Verde, dust LW forcing efficiency for this study was found to be a factor of two larger stemming from differences in environmental and surface conditions, aerosol absorption, and Zhangye's close proximity to major desert sources. Relative to observed and modeled ranges in surface DRE_{LW} for clouds (~30–80 Wm^{-2}) and greenhouse gases (~2 Wm^{-2}), this study's upper range in DRE_{LW} represents a significant perturbation to the climate system with important implications for better understanding regional changes in surface temperatures and moisture budgets.

Citation: Hansell, R. A., et al. (2012), An assessment of the surface longwave direct radiative effect of airborne dust in Zhangye, China, during the Asian Monsoon Years field experiment (2008), *J. Geophys. Res.*, *117*, D00K39, doi:10.1029/2011JD017370.

1. Introduction

[2] During springtime, dust outbreaks frequently occur over the Gobi and Taklamakan Deserts in Northwest China

[1]ESSIC, University of Maryland, College Park, Maryland, USA.
[2]NASA Goddard Space Flight Center, Greenbelt, Maryland, USA.
[3]Science Systems and Applications, Inc., Lanham, Maryland, USA.
[4]NASA Ames Research Center, Moffett Field, California, USA.
[5]College of Atmospheric Sciences, Lanzhou University, Lanzhou, China.
[6]Department of Atmospheric and Oceanic Sciences, University of Maryland, College Park, Maryland, USA.
[7]Institute of Atmospheric Physics, Chinese Academy of Sciences, Beijing, China.

Corresponding author: R. A. Hansell Jr., ESSIC, University of Maryland, College Park, MD 20740, USA. (richard.a.hansell@nasa.gov)

[*Tsay*, 2009] contributing up to one-third of the global-annual dust burden [*Zhang et al.*, 1997]. Once airborne, dust can be transported over various length scales where it can interact with other aerosols and clouds and affect the radiative energetics of the earth-atmosphere system. Consequently, dust aerosols can modulate regional climate patterns such as changes in precipitation [*Yoshioka et al.*, 2007; *Menon et al.*, 2002] and the evolution of the hydrological cycle where shifts in the onset of the Asian Monsoon have been reported [*Lau et al.*, 2006].

[3] Many recent studies have focused on the shortwave (SW) radiative impacts of dust and other aerosols (e.g., soot) across China. For example, *Z. Li et al.* [2010] examined regional radiation budgets at 25 ground stations distributed across the country, and found that aerosols strongly affect the absorption of the atmosphere. *Liu et al.* [2008] and *Ge et al.*

[2010] evaluated the SW optical properties and radiative effects of dust in the Northwest regions of Yinchuan and Zhangye, respectively. Further, *Huang et al.* [2009] and *Xia and Zong* [2009] both used satellite observations to investigate the SW radiative impacts over the Taklamakan Desert. Although the latter two works also assessed longwave (LW) impacts (e.g., *Huang et al.* [2009] used standard dust aerosol spectral optical properties constrained with observationally derived optical depth and single-scattering albedo in the solar to gauge the LW effects), it appears, to the best of our knowledge, that not many studies of the DRE_{LW} of dust have been conducted in this region, particularly using surface-based measurements. Clearly, better knowledge of this parameter is vitally necessary for climate studies in order to gauge the diurnal effects of dust aerosols. Although, globally, studies of DRE_{LW} are increasing [e.g., *Haywood et al.*, 2005; *Highwood et al.*, 2003; *Hsu et al.*, 2000; *Zhang and Christopher*, 2003; *Hansell et al.*, 2010], investigations remain to be a challenge due to the paucity in LW dust optical properties and the low signal-to-noise ratio in LW broadband measurements [*Highwood et al.*, 2003].

[4] In this study, we seek to answer a fundamentally important question, namely what is the DRE_{LW} of dust aerosol for areas located near the major desert source regions in China. Moreover, exploiting the strength of ground-based sensors, what is the magnitude of DRE_{LW} and how significant is it relative to its SW counterpart. Since LW perturbations to the surface energy budget can have important implications for its effects on surface temperatures, soil moisture, and the stability of the atmosphere, this work is essential particularly in those areas where dust aerosol is prevalent.

[5] In this study we exclusively focus on the DRE_{LW} of dust at Zhangye, a semi-arid region inside the Hexi Corridor region of northwest China, an effort that was part of the overlying Asian Monsoon Years 2008 (AMY08) research initiatives project [*Lau et al.*, 2008]. Details regarding the observation networks deployed in China in support of the East Asian Study of Tropospheric Aerosols and Impact on Regional Climate (EAST-AIRC) can be found in *Li et al.* [2011]. Using an air mass back trajectory model, *Ge et al.* [2010] identified two main transit paths of dust into Zhangye – a westerly path across the Taklamakan Desert, and a northwesterly path through the Gobi Desert, in addition to contributions from localized dust. Due to its close proximity to these major desert sources, it is evident that Zhangye is at the center of extensive dust activity. Taking advantage of a unique and comprehensive data set, this study offers an unprecedented glance into the DRE_{LW} of Asian dust.

[6] Here we use the combined data from radiative transfer modeling and a comprehensive network of ground-based sensors from NASA Goddard's ground-based mobile laboratories: Chemical, Optical, and Microphysical Measurements of In situ Troposphere (COMMIT) and Surface-sensing Measurements for Atmospheric Radiative Transfer (SMART). The SMART-COMMIT laboratories (http://smartlabs.gsfc. nasa.gov/) were deployed to Zhangye (39.0°N; 101°W) at an altitude of ~1.5 km (850 mb) above sea level (ASL) from April–June 2008 as part of one of the field experiments to the AMY08 study - the U.S. Department of Energy (DOE)

Atmospheric Radiation Measurement Mobile Facility in China (AMF-China) [*Li et al.*, 2011].

[7] Both the surface and top-of-atmosphere (TOA) components of DRE_{LW} are evaluated with emphasis given to the surface contributions to complement previous works [e.g., *Highwood et al.*, 2003; *Hsu et al.*, 2000] and to facilitate comparisons between regions exhibiting very different surface properties and environmental conditions. Here we compare the instantaneous DRE_{LW} (Wm^{-2}) and forcing efficiency ($Wm^{-2}\tau^{-1}$) at Zhangye, a land desert site, with those from Cape Verde Island, an oceanic maritime site, during the NAMMA-2006 field study on Saharan dust [*Zipser et al.*, 2009; *Hansell et al.*, 2010]. This work also evaluates regional heating rate profiles to address radiative impacts over the atmospheric column and lastly, the significance of the LW contributions relative to the shortwave DRE is examined. Here the DRE_{LW} of dust are given as instantaneous values for cloud-free atmospheres.

[8] Key instruments and data from SMART-COMMIT used in this study include the following: Bomem AERI (LW spectral radiances), TSI APS-3321 (Coarse-mode particle size spectra), TSI TEOM (PM_{10} mass concentrations), and Eppley Precision Infrared (PIR - LW broadband irradiances), as well as the AERONET [*Holben et al.*, 1998] Sun photometer and MPLNET [*Welton et al.*, 2001] micro-pulse lidar (MPL). Details of these instruments, their specifications and associated data products can be found at: http://smartlabs. gsfc.nasa.gov/.

[9] Using the AERI system, an IR interferometer that is sensitive to the atmosphere's downwelling thermal emissions, both daytime and nighttime radiative effects are examined using the dust detection and retrieval methodology from *Hansell et al.* [2008]. Time series of retrieved aerosol optical thickness (AOT) from AERI along with local measurements of surface irradiances and atmospheric state, serve as constraints to the radiative transfer model (RTM), from which instantaneous DRE_{LW} and heating rates are calculated.

[10] Appropriate for this region, a dust optical model was constructed based on local soil mineralogy results reported by *Jeong* [2008]. Dust particle sizes were characterized by measurements from COMMIT's ground-based aerodynamical particle sizer (APS-3321) and for simplicity, particle shapes were assumed to be homogeneous and spherical, although it is well known that dust particles, particularly course-mode dust, exhibit a myriad of more complex, nonspherical geometries [*Nousiainen*, 2009]. For calculating radiative fluxes however, this assumption should not introduce significant errors [*Mishchenko et al.*, 1995]. *Fu et al.* [2009], for example, reported relative errors of less than 5% in the SW when applying spherical assumptions to dust. The relative error is even smaller in the LW since radiative transfer is dominated by absorption with less sensitivity of the scattering phase function to particle shape. Since DRE is a relative energetic parameter (i.e., relative to clear-sky), estimated errors in DRE due to spherical approximations are taken to be much less than 5%.

[11] The organization of this paper is as follows. An overview of regional dust measurements and data at SMART-COMMIT are given in section 2. Details of soil mineralogy are presented in section 3 while section 4 describes the methodology and DRE computations using
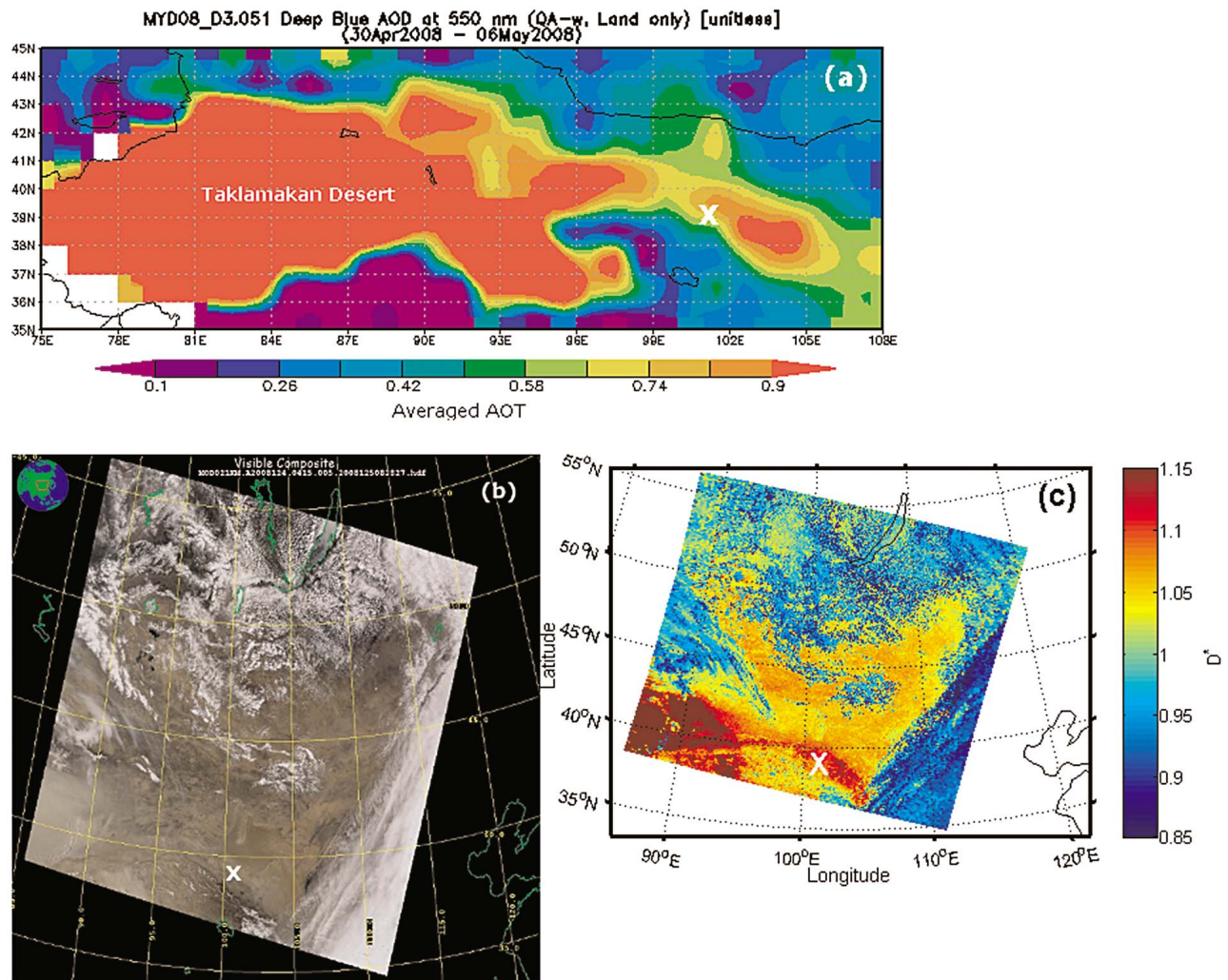
Figure 1. (a) Aqua MODIS Deep Blue averaged AOT at $\lambda = 0.55 \ \mu$m (from the NASA Giovanni system, courtesy of NASA GES DISC) during most active dust period of deployment. (b) Terra MODIS Level-1b visible image showing heavy dust activity on 3 May 2008 at 0415 UTC and (c) D* parameter for the same MODIS granule separating dust and cloud fields. White crosses in each panel mark the location of SMART-COMMIT at Zhangye. See text for details.

the radiative transfer model. The study's results of dust optical properties and DRE are discussed in section 5 and lastly, a summary is given in section 6.

2. Regional Dust Measurements and Data

[12] Figure 1a, produced from NASA's Giovanni system, shows a regional map of Deep Blue averaged AOT from the MODerate-resolution Imaging Spectroradiometer (MODIS) aboard the Aqua satellite for probably the most active dust period of the field study – 30 April through 6 May. Inside the dust plume downwind of the Taklimakan Desert is the deployment site at Zhangye (white cross). Given the site is located within the Hexi Corridor, high dust loading (color-coded yellow and red) is prevalent throughout most of the area, making Zhangye an ideal location for investigating dust DRE_{LW}. A Terra MODIS Level-1b visible granule from 3 May at 0415 UTC (Figure 1b) reveals a tan-colored layer of heavy dust skirting the bottom of the image. The white

cross again marks the deployment site inside the plume path. To enhance the dust further, the D* parameter [*Hansell et al.*, 2007], a dust detection parameterization using brightness temperature differences across the LW channels, was employed to separate dust and cloud fields for the same MODIS granule where D* ≥ 1 denotes dust and D* < 1 denotes cloud. The D* map (Figure 1c) reveals an intense dust plume emanating from the Taklamakan Desert and crossing over into Zhangye (white cross). *Wang et al.* [2010] also examine the same time period using Aerosol Index values from the Ozone Monitoring Instrument aboard the Aura satellite and show the evolution of strong dust plumes over this region. During this period, SMART-COMMIT was fully operational capturing distinct transitions in dust loading just prior to and throughout the heavier events in the early part of May.

[13] Presented in Figure 2a is an example of daily 3-h-averaged AERI spectral radiances (v = 800–1200 cm^{-1} in the wave number domain) at Zhangye from 22 April–7
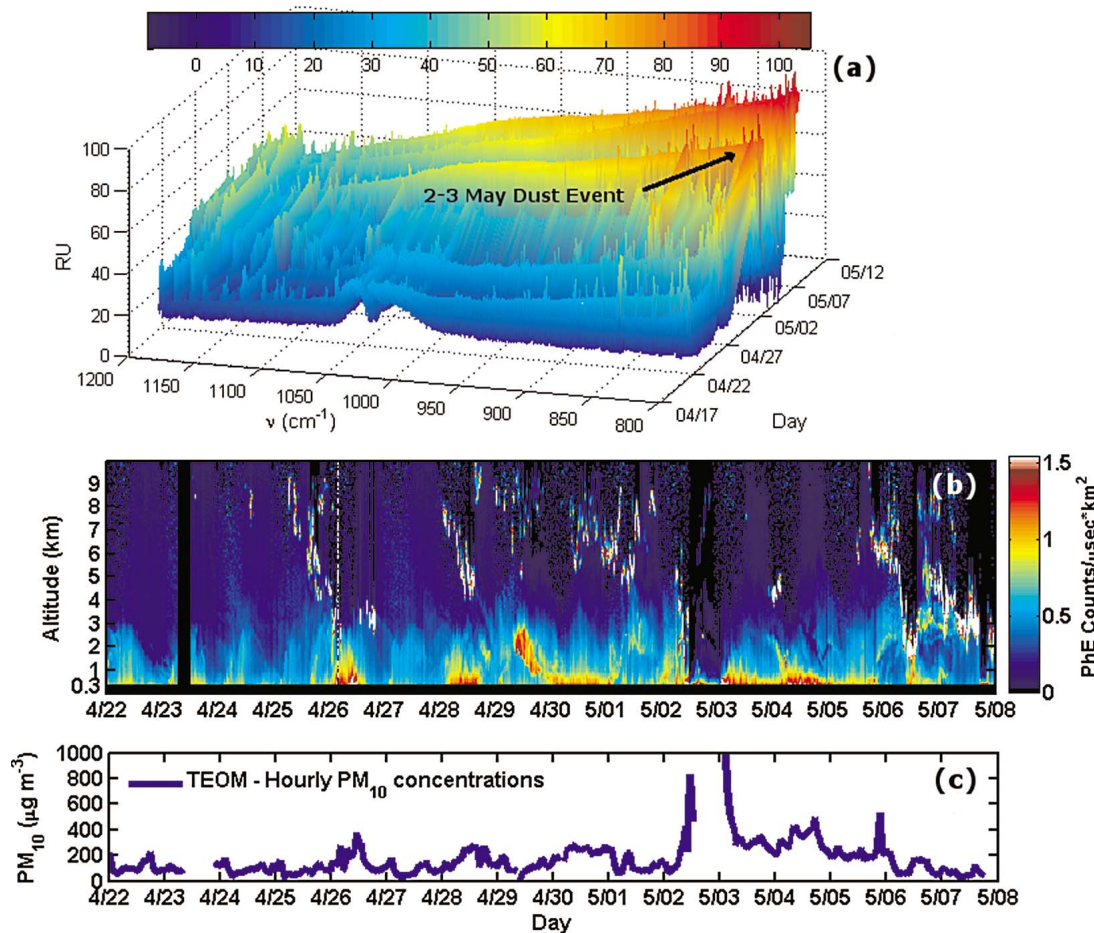
Figure 2. (a) AERI measured radiances (radiance units, RU = mW m^{-2} sr^{-1} cm^{-1}) from 800 to 1200 cm^{-1} at Zhangye China during active dust period. Spectral features due to ozone, water vapor, and cloud are also evident. (b and c) The MPL NRB profiles and TEOM PM$_{10}$ mass concentrations, respectively over the same period in Figure 2a. NRB data in Figure 2b are in raw photon counts (PhE Counts/μsec*km^2). See text for details.

May. Along with dust, the spectra exhibit a range of absorption features including those from ozone (1050 cm^{-1}), the water vapor continuum, and clouds. Intensity peaks from dust can be seen around 2–3 May (denoted by the black arrow) followed by those due to clouds at the end of the time series. Magnitude differences in measured spectral radiances between Zhangye and Cape Verde [*Hansell et al.*, 2010] are strongly linked to differences in the atmospheric temperature and humidity profiles and dust mineralogy.

[14] For qualitative purposes, aerosol and cloud normalized relative backscatter (NRB) profiles (in raw photon counts - PhE Counts/μsec*km^2) and hourly PM$_{10}$ aerosol mass concentrations (in μg/m^3) from a collocated MPL (http://mplnet.gsfc.nasa.gov) [*Welton et al.*, 2001] and TEOM, respectively, are shown in Figures 2b and 2c. PM$_{10}$ mass concentrations are derived via in situ measurements, using a Tapered Element Oscillating Microbalance (TEOM) Series 1400ab from R&P Co. which captures the particles on filter paper for further analysis. TEOM measured PM$_{10}$ mass concentrations yield the total mass of particles having an upper size cut of 10 μm. The MPL data reveals a strong presence of surface dust throughout much of the period with elevated layers reaching altitudes as high as ~3 km (e.g.,

29–30 April). Note that the heavier dust event in early May was not captured by the MPL due to the window becoming dirty; however, this strong event is clearly evident in the TEOM data set (Figure 2c) shown by a marked increase in aerosol concentration levels. PM$_{10}$ and AOT generally are linearly correlated with each other. In this study, r~0.68 while in other studies [e.g., *Péré et al.*, 2009; *Chaudhry et al.*, 2007] r ranges from 0.67 to 0.79. However, the purpose of introducing the MPL and TEOM data is not for conducting quantitative assessments but rather to provide qualitative insight as to the changes and magnitudes of these parameters. Clouds are also apparent during the deployment ranging from low-level stratus to mid- and upper-level cirrus.

[15] Retrieved temperature and moisture profiles from AERIPLUS, a physical retrieval algorithm using AERI radiances as input, were used to specify the temporally resolved thermodynamic structure of the boundary layer with an accuracy in temperature to better than 1 K and approximately 5% in absolute water vapor when compared to well calibrated radiosondes [*Feltz et al.*, 2003]. These profiles were later used to constrain both the aerosol retrieval algorithm and RTM for calculating broadband irradiances.

Table 1. Regional Dust Minerals

Jeong [2008]	Current Study	Data Source
Quartz (41%)	quartz (43%)[a]	Gray [1963], Drummond [1935], Spitzer and Kleinman [1961], Philipp [1985], and Longtin [1988]
Plagioclase (17%)	anorthosite (17%)	Aronson and Strong [1975], LW
K-Feldspar (9%)	andesite (8%)[a]	Pollack et al. [1973], SW
Calcite (10%)	calcite (10%)	Long et al. [1993], LW; Marra et al. [2006], SW
Mica (12%)	mica (12%)[b]	Aronson and Strong [1975], Muscovite (LW); Egan and Hilgeman [1979], Illite (SW)
Chlorite (10%)	chlorite (10%)	Mooney and Knacke [1985], LW; Thomas and Gautier [2009], SW
Amphibole (1%)	amphibole (0)[a]	no data available[a]
Dolomite (0)	dolomite (0)	N/A[c]
Gypsum (0)	gypsum (0)	N/A[c]
Total – 100%	total – 100%	N/A[c]

[a]Weightings adjusted to account for differences in available data.
[b]Micas consist of equal weightings of muscovite (6%) and illite (6%).
[c]N/A, not applicable (mineral not identified at Zhangye).

Due to Zhangye's inland location and lack of moisture supply, the atmosphere was found to be quite dry (<20% RH) with the more active dust periods (e.g., early May) coinciding with drier air masses.

[16] Later in section 5, AERONET [Holben et al., 1998] Level 2 retrieved AOTs (quality assured and cloud-screened) are compared to those from AERI. Further details of AERONET can be found at http://aeronet.gsfc.nasa.gov. Additionally, the performance of the RTM is validated by comparing downward LW irradiances with those from a collocated PIR (http://smartlabs.gsfc.nasa.gov/) which measures hemispherical broadband surface irradiance (3.5–50 μm).

3. Regional Dust Mineralogy

[17] A spherical dust microphysical model using SMART-COMMIT measured size distributions and spectral refractive indices ($\lambda = 2.5$–39 μm) based on prior mineralogy studies from the region formed the primary aerosol inputs to the RTM. The composition of Asian dust at Zhangye is reconstructed using the mineralogical results presented in Jeong [2008]. The latter study performed a comprehensive comparative analysis of measured dust samples in Korea with soil samples collected from various source regions in China. The optical constants of minerals nearest to those reported in Jeong [2008, Table 1] for Zhangye (Silt-B) are internally combined to yield a representative mixture for the region. A summary of the minerals employed in this study is provided in Table 1.

[18] Key components sorted by relative weight percentage are quartz (43%), calcite (10%), chlorite (10%), plagioclase (anorthosite + andesite – 25%), and mica (muscovite + illite – 12%). Assuming spherical shapes, these minerals are internally mixed using the Bruggeman approximation found in the effective medium code from Ossenkopf [1991]. Following C. Li et al. [2007, 2010], the presence of soot from local pollution was also accounted for by volume weighting the resulting mixture with 2% black carbon using the optical constants from Shettle and Fenn [1979].

[19] It is noted that some of the mineral data sets used only covered the SW but not the LW and vice versa (Table 1). Consequently alternate data sources were required to complete the spectral coverage needed. For example, the complex refractive indices of calcite at the short wavelengths derived by Marra et al. [2006] were employed to complement the

LW values from Long et al. [1993]. Although the former values are known to be ~3 orders of magnitude greater than those reported in other works [e.g., Roush, 2010], i.e., the absorption is large, the computed bulk single-scattering albedo ($\lambda = 0.5$ μm) for this study is still highly scattering. We discuss probable causes and their effects later in this section. For the plagioclase minerals, andesite and anorthosite are used to cover the SW and LW spectral regions, respectively. Andesite is an igneous rock, dominated by plagioclase, but also contains other minerals, including the possibility of K-bearing feldspars while anorthosite is an igneous rock composed of 90–100% plagioclase feldspar with a minimal mafic component of 0–10%.

[20] For mica, the minerals illite and muscovite are used to cover the SW and LW regions, respectively. Last the SW refractive indices for chlorite presented in Thomas and Gautier [2009] complement those from Mooney and Knacke [1985] at the longer wavelengths. For values of
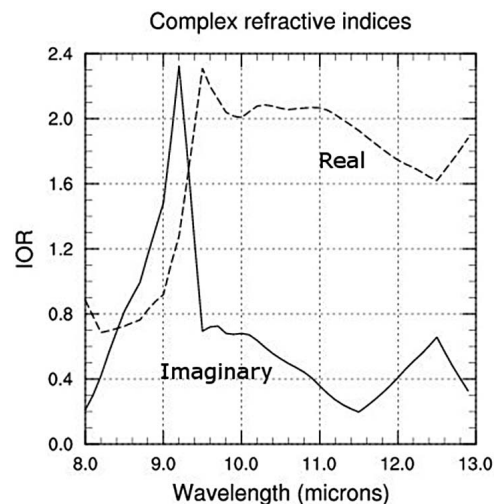
Figure 3. Re-constructed optical constants based on soil mineralogy results at Zhangye from Jeong [2008] where both real and imaginary spectral components are shown. The y axis (index of refraction, IOR) represents both real and imaginary terms. The strong absorptive peak near 9 μm reveals silicates are dominant soil minerals in the dust mixture. See text for details.
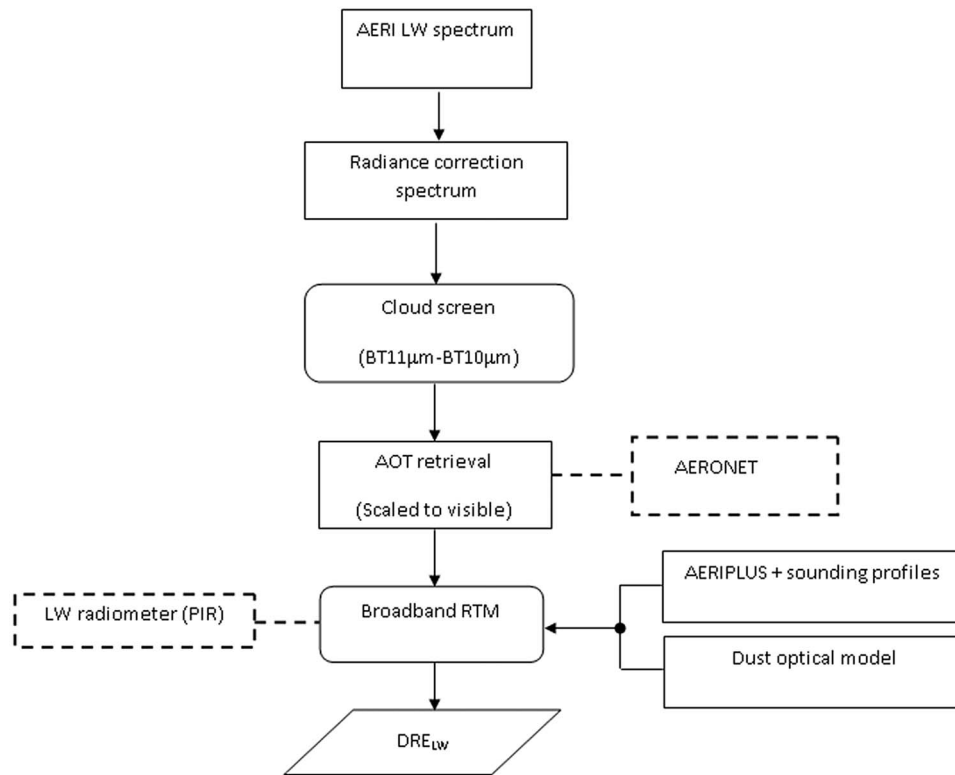
Figure 4. Flowchart illustrating methodology for assessing DRE_{LW}.

chlorite that lie in between these two data sets ($\lambda = 1.6$ and 2.19 μm), the refractive indices are assumed to be equal to the nearest neighboring points since the changes in refractive index are shown to be nearly constant with wavelength. The resulting complex spectral refractive indices ($m = m_r + im_i$) for this study (Figure 3) reveal a large absorption peak around $\lambda = 9.2$ μm, and a secondary peak around $\lambda = 12$ μm, both characteristic of silicates, notably quartz, which appear to be the dominant minerals for this region [*Jeong*, 2008].

## 4. Methodology and Radiative Transfer Calculation of DRE_{LW}

[21] The field study took place from 13 April through 21 June 2008. In this work, we examine the earlier part of the deployment focusing on the period from 19 April through 6 May when dust activity peaked. As seen by the measurements in Figure 2, variable but persistent dust loading offered a unique opportunity for probing the region's DRE. A flow-diagram summarizing the methodology, based on *Hansell et al.* [2010], is given in Figure 4. Note that the solid/dashed boxes distinguish between the operational/ validation steps of the methodology, respectively. From top to bottom, each element of the diagram is briefly explained below.

[22] First the AERI data is read in followed by a radiance correction scheme that is applied to the nearly 59,000 spectra to account for the nonlinear effects associated with AERI's channel-1 HgCdTe detector [*Hansell et al.*, 2008]. Next, a

cloud and dust detection technique based on the brightness temperature slope between $\lambda = 10$ μm and $\lambda = 11$ μm of the corrected AERI spectrum is used to separate dust from clouds. Consequently, a total of 7,400 spectra classified as cloud were rejected ($\sim$12%). In addition to the cloud filter, the cases were also checked using the MPL NRB profiles and AERONET Level 2 quality assured/cloud screened data. After applying the detection scheme, the remaining spectra were inputted into the retrieval code yielding a time series of LW ($\lambda = 10$ μm) AOT, later scaled to $\lambda = 0.55$ μm, at a temporal resolution of approximately 90 min. For validation purposes, this is compared with the AOT time series from AERONET. Last the retrieved AOT data along with combined AERIPLUS/sounding profiles (for characterizing changes in atmospheric state), and constructed dust model were used in the broadband RTM to calculate downwelling (I$\downarrow$) and upwelling (I$\uparrow$) LW irradiances at the surface and TOA. Modeled downwelling irradiances are then compared with measurements from a collocated PIR finally followed by the computation of DRE. Here, DRE is defined as:

$$DRE = \left(I_{all-sky}\downarrow - I_{all-sky}\uparrow\right) - \left(I_{clear-sky}\downarrow - I_{clear-sky}\uparrow\right) \quad (1)$$

which is the net difference in irradiance between all-sky (aerosols + gases) and clear-sky (gases only) conditions. Since the calculated DRE using net versus downward irradiance in equation (1) only introduced a difference of $\leq$0.15 Wm^{-2} (on average over the analysis period), the upward irradiance component is not considered in this study. Observed clear-sky references were not available due
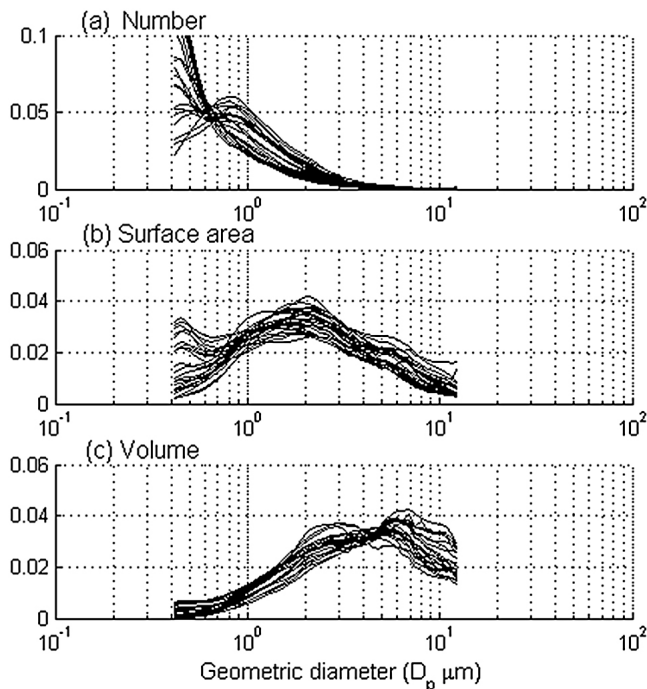
Figure 5. APS normalized size distributions for (a) particle number ($dN/dlnD_p$), (b) surface area ($dA/dlnD_p$), and (c) volume ($dV/dlnD_p$) versus geometric diameter. See text for details.

to the near daily presence of clouds and/or aerosol, thus references had to be calculated using the analyzed atmospheric profiles derived from AERIPLUS and soundings with dust and cloud optical depths set to zero.

[23] In this study we use the NASA Langley modified Fu-Liou 1-D RTM (version FL0403 15 April 2003 [*Rose and Charlock*, 2002; *Fu and Liou*, 1992, 1993; *Huang et al.*, 2009]) to calculate broadband irradiances for both dust and pristine conditions. Applying the analytical solution of the four-stream radiative transfer scheme, this model runs very fast and accurately across fifteen SW spectral bands from 0.175 to 4.0 μm and twelve LW bands between 2850 and 0 cm^{-1}. The correlated k-distribution method is used to account for non-gray gaseous absorption due to H_2O, CO_2, O_3, N_2O, and CH_4 [*Fu and Liou*, 1992]. The code also employs a parameterized version of the LW water vapor continuum model (CKD2.4) to account for strong water vapor absorption. Dust AOT in the model calculations was based on AERI retrieved values scaled from $\lambda = 10$ μm to $\lambda = 0.55$ μm using a LW-to-visible extinction coefficient ratio [$\beta_{ext}(10$ μm$)/\beta_{ext}(0.55$ μm$)$] of ~0.5, following previous works including *Hansell et al.* [2011]. Modifications to the code enable inputting retrieved AOT and combined AERIPLUS and radiosonde profiles of pressure, temperature, and water vapor density to compute irradiances at the surface and TOA. Dust optical properties are prescribed to be uniform and homogeneous inside each layer and the dust vertical distribution was set to an AOT scale height of 3 km, roughly corresponding to that observed by the MPL. The University of Wisconsin's Global IR Land Surface Emissivity database

[*Seemann et al.*, 2008] (http://cimss.ssec.wisc.edu/iremis/) was used to determine an averaged LW ($\lambda = 8$–12 μm) emissivity ($\varepsilon_\lambda = 0.96$) of the local soil during the months of April–May 2008 and following *Ge et al.* [2010] an averaged broadband surface albedo of 0.21 was employed. Last the temporal variability of the thermodynamic state parameters (i.e., temperature/relative humidity) are accounted for by combining AERIPLUS [*Feltz et al.*, 2003] profiles for the first 4 km in the model atmosphere, with averaged regional sounding data from meteorological stations near Zhangye (Minqin and Jiuquan), up to a height of ~18 km. For levels above 18 km, a climatological midlatitude summer profile [*McClatchley et al.*, 1972] was employed.

5. Results: Optical Properties and DRE_{LW}

[24] The derived dust optical properties are first examined followed by an uncertainty analysis to quantify the sensitivity of modeled downwelling LW irradiances to various critical parameters. Next comparisons are presented between the retrieved AOT and those from a collocated AERONET Sun photometer using cloud-screened and quality assured Level 2 data. This is then followed by validation of the RTM's performance relative to broadband LW irradiances measured at the site. Last, the DRE_{LW} results including their surface and TOA components, heating rate profiles, and the LW/SW ratio for gauging LW significance are given. We point out that compared to the SW forcing efficiencies, those in the LW, which we later use for comparisons, are less robust due to a greater sensitivity to the local environment.

5.1. Optical Properties

[25] For the study period, COMMIT's APS measurements of number-size distributions were averaged and used to calculate the bulk single-scattering properties (SSP) across the RTM spectral bands (section 4). Figures 5a–5c show the measured APS size distributions for particle number, surface area, and volume, with average geometric sizes of about 0.9, 1.1, and 2 and 6 μm, respectively. Calculated SSP (extinction coefficient - β_{ext}, asymmetry parameter - g, and single-scattering albedo - ϖ) based on the minimum (red curve), maximum (black curve), and mean (green curve) number size distributions are presented in Figure 6. Note that the SW single-scattering albedos shown in Figure 6c are higher than what are typically found in literature. For example, *Ge et al.* [2010] report single-scattering albedos in the range of $\varpi = 0.74$–0.8 at $\lambda = 0.5$ μm versus $\varpi = 0.96$ for this study. Plausible reasons for this difference include (1) not having enough absorbing anthropogenic aerosols (e.g., soot) and/or iron oxides (e.g., hematite and goethite) in the optical model (2) the inability to model the exact mixing state and mineralogy of the local dust, (3) potential uncertainties in the optical constants [e.g., *Roush et al.*, 2007] that can propagate into the calculated SSP, and (4) possible uncertainties in the regional dust samples. *Jeong* [2008] reported that some clay aggregates were associated with iron oxides which can certainly account for the stronger absorption at the shorter wavelengths. Likewise, *Kim et al.* [2004, 2005] claimed that low ϖ values ($\varpi \sim 0.80$) downwind of the dust source regions in China could be due to extensive mixing of dust with polluted air masses. As shown by the blue curve in
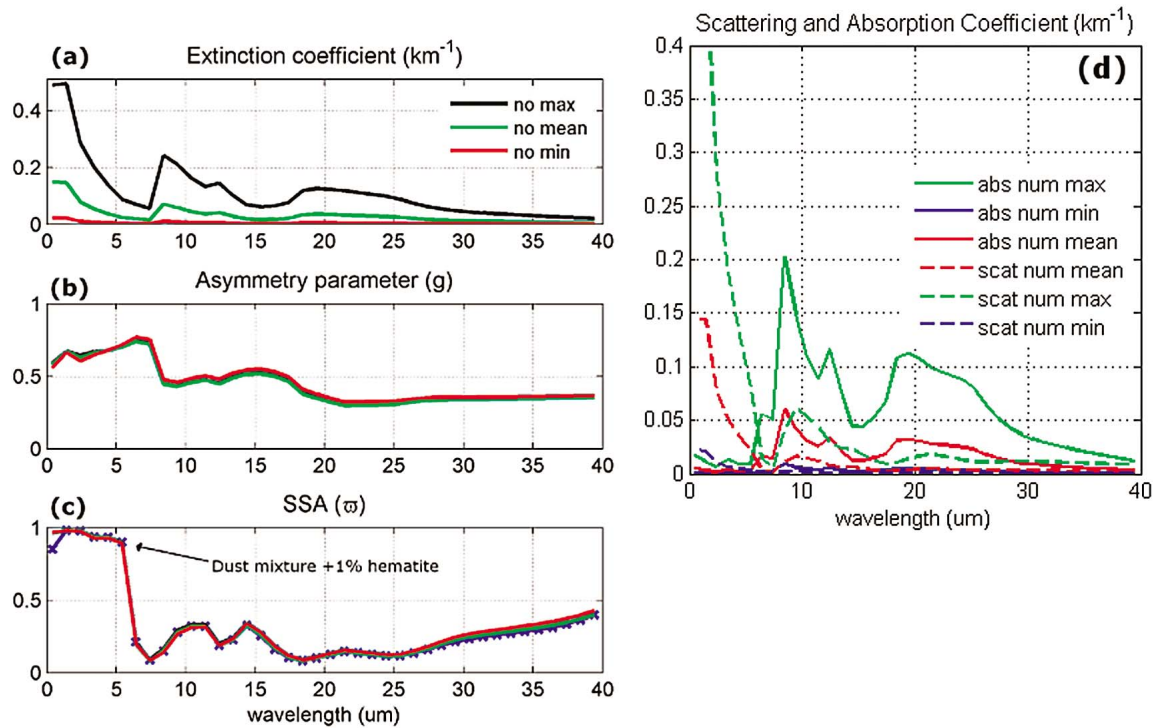
Figure 6. Spectral single-scattering properties for regional dust including (a) extinction coefficient, β_{ext}; (b) asymmetry parameter, g; and (c) single scattering albedo, ϖ. The three curves (green, black, and red) correspond to each parameter using the mean, minimum, and maximum size distributions, respectively over the study period. Blue curve in Figure 6c is the composite dust mixture with 1% hematite added. (d) Comparisons of spectral scattering and absorption coefficients for the same size statistics. See text for details.

Figure 6c, adding hematite [*Longtin*, 1988] or increasing the amount of soot [*Shettle and Fenn*, 1979] in the model by 1% resulted in ~10% decrease in ϖ at $\lambda = 0.5 \ \mu$m (i.e., $\varpi \sim 0.87$). Small changes in absorption were also found throughout the LW ($\lambda \sim 30$–$40 \ \mu$m) but not enough to impact the DRE_{LW} results (see section 5), hence we employ the optical model as shown in Figure 6.

[26] The largest range in optical properties due to particle size changes is most evident in the magnitude of β_{ext} (Figure 6a). Differences in g and ϖ (Figures 6b and 6c, respectively) are less obvious but do reveal small differences. For example at 10 μm, a strong absorption frequency for dust minerals, both parameters vary by about 6%. For comparison (not shown), ϖ employed in the NAMMA study based on the spectral refractive indices of *Volz* [1973] for transported Saharan dust, is on average about 50% larger (i.e., more scattering) in the LW relative to the current study ($\varpi = 0.47$ versus 0.26). Hence for this study, dust absorption at Zhangye was found to be larger and will therefore contribute more to the downwelling LW emissions at the surface. The significance of this point is examined later in this section. It is also interesting to point out that *Huang et al.* [2009] reported Taklamakan dust aerosols to be more absorbing (~6%) at the shorter wavelengths ($\lambda = 0.67 \ \mu$m) than Saharan dust. The spectral scattering and absorption coefficients for each size distribution in the LW are presented in Figure 6d, with the broken/solid curves denoting scattering/absorption, respectively. Not surprisingly, scattering

dominates at the shorter wavelengths, while absorption contributes more in the LW, most notably around 10 and 20 μm. Note that the values shown are based on Mie spherical solutions. For detailed discussions on the effects of non-sphericity in the LW, refer to *Hansell et al.* [2011].

5.2. Uncertainty Analysis

[27] Sensitivity of LW surface irradiances to key atmospheric, dust aerosol, and surface parameters include boundary layer temperature and relative humidity, particle absorption, particle size, and dust layer scale height. The resulting uncertainties are summarized in Table 2. Downwelling LW irradiances are practically insensitive to

**Table 2.** Uncertainty Analysis of Model Irradiances

Parameter	Perturbation	Uncertainty (Wm^{-2})
Particle size[a]	minimum, mean, and maximum SD	0.7 ± 0.4
Temperature[b]	±2 K	10.9 ± 1.1
Water vapor[c]	±20%	3.3 ± 1.3
Dust absorption[d]	±20%	2.2 ± 1.3
Dust altitude	scale height: 1–5 km	2.0 ± 1.2

[a]APS measured size distributions (SD) during study period. Refer to Figure 4.
[b]Temperatures adjusted ±2 K over lower most layers (740–850 mb).
[c]Water vapor amounts adjusted ±20% over lower most layers (740–850 mb).
[d]Model spectral absorption coefficients and SSA (see text).
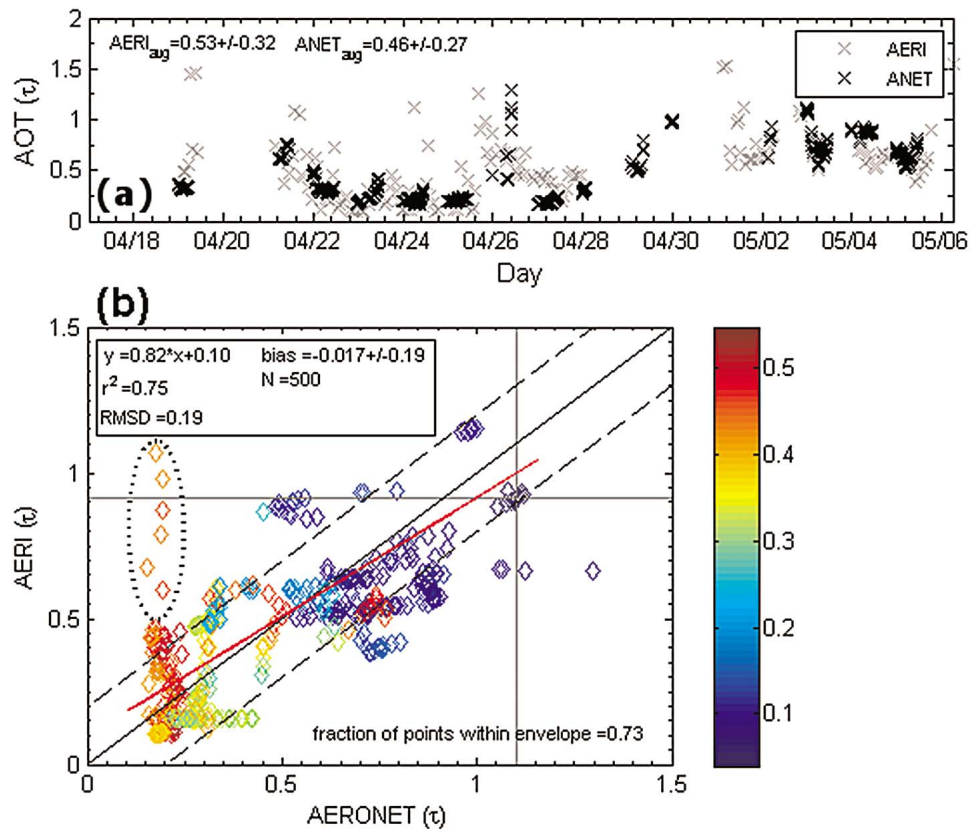
Figure 7. (a) Time series of AERONET (black markers) and AERI (gray markers) retrieved AOT when dust was active and (b) AOT scatterplot (AERI versus AERONET) over same period where N represents the number of AERI points interpolated to AERONET. Points are color-coded according to the AERONET Ångström exponent. Circled region likely corresponds to overestimated water vapor. Solid line at center is the 1:1 line; outer dashed lines represent region bounded by AERONET AOT values ± 0.20; red line is the linear best fit and intersecting gray lines mark maximum AOT value from May 3rd dust event. See text for details.

surface emissivity and are therefore not included in the analysis. Perturbations in each parameter are made relative to the region's thermodynamic profiles, derived single-scattering properties, dust layer scale heights, and particle size spectra. Adjustments are made in the boundary layer temperature and water vapor profiles over a pressure range of 780–845 mb in amounts consistent with published measurement uncertainties of around ±2 K and ±20%, respectively [e.g., *Aumann et al.*, 2003]. Changes in particle absorption are assessed by varying the spectral absorption coefficients and single-scattering albedos in the optical model by ±20%. Particle size uncertainties are based on the range of observed size distributions and lastly, dust layer scale heights are computed over a range of 1–5 km. For the prescribed ranges, the largest uncertainties in LW irradiance occur from changes in the atmospheric state parameters, particularly temperature, followed by aerosol absorption and dust altitude (Table 2). Measurements also exhibit uncertainties and were found to be on the order of 1% ($\sim$2–3 Wm^{-2}) based on comparisons of broadband irradiance data from collocated ground-based PIRs. Considering both measurement and model uncertainties, we take the

combined uncertainty to be on the order of ±15 Wm^{-2} or within 5–7%.

5.3. Retrieved AOT

[28] Figure 7a presents the total (daytime + nighttime) scaled AOT from AERI (gray symbols) compared with those from collocated AERONET retrievals (black symbols) at $\lambda =$ 0.55 μm for the period 19 April–6 May. A few data void periods for both instruments are evident. First, it is noted the start times of both data sets begin on 19 April corresponding to when AERI began operating. Second, clouds were ubiquitous from $\sim$19–21 April; hence the cloud filter schemes for both instruments rejected most of the data points during this period. For the same reason, data was also removed from 30 April–1 May. Third, from $\sim$28–30 April, the AERI data acquisition was interrupted due to a system error. The system was subsequently restarted and was back online as of 1 May. Note that the retrieved AOT from AERI is more representative of extinction near the surface, since most of the detected IR signal comes from lower atmospheric emissions [*Feltz et al.*, 2003].

[29] Compared to AERONET, AERI is able to observe the daytime variability in dust loading reasonably well with a

mean AOT of $\tau = 0.53 \pm 0.32$ (1-σ standard deviation), compared to $\tau = 0.46 \pm 0.27$ for AERONET, where the mean value is within 15% of that from AERONET. Although both instruments view the atmosphere from different viewing angles, they effectively see the same dust region since dust is for the most part uniformly distributed in space (compared to cloud), particularly near the source region. Also, differences in wavelengths over which the instruments sense the atmosphere (SW versus LW) are accounted for by applying a LW-to-visible extinction coefficient ratio to the AERI data. Overall, the results are encouraging and show good agreement in the observed dust trends.

[30] Both instruments observed relatively low AOT levels from about 23–25 April, coincident with a water vapor minimum, followed by a sharp increase in dust loading starting at the end of April and proceeding into early May culminating with the large dust episode between 2 and 3 May. Note that there are a few large AERI retrieved AOT (>1) during this period, which could be due to overestimated water vapor in the model profiles and/or missed clouds in the detection scheme. The analysis period stops at 6 May since clouds became more prevalent near the site.

[31] A scatterplot of AERI and AERONET retrieved AOT values, which have been color-coded according to the Ångström exponent, a proxy for particle size, is presented in Figure 7b. Note that the AERI values have been interpolated to the AERONET observation times (N = 500 total points). As shown, higher aerosol loading points (blue markers) have a lower Ångström exponent (<0.2) suggestive of larger sized particles, mostly dust. Likewise points with low to intermediate dust loading exhibit higher Ångström exponents (>0.2) indicative of relatively smaller particles which may be due to dust and/or pollution aerosols. The negative correlation is consistent with previous studies (e.g., *Nurhayati and Nakajima*, 2012 and references therein). The higher retrieved values from AERI (circled region) are from 24 April and could be due to uncertainties in the retrieved water vapor amounts (this coincides with the driest period of the deployment) and in the retrieval itself. Overall the slope of the linear regression relative to the 1:1 line is about 0.82 but increases to 0.88 if the offset is forced through zero. Here the offset is related to retrieval uncertainties when AOT = 0. The comparison yields a linear correlation coefficient of 0.75 with an RMSD of 0.19 and an average bias of -0.017 ± 0.19 (1-σ standard deviation) over the period examined. Here, RMSD is a qualitative indicator of retrieval accuracy while average bias is defined as the mean value in residuals between the modeled and observed data. The number of retrieved points inside the expected error envelope of AERONET observations is around 73% (i.e., 73% of AERI AOT values are within an expected error of AERONET observations given by $AOT_{AERONET} \pm 0.20$). Last, the mean nighttime AOT was found to be nearly equal to its daytime value ($\tau = 0.53$), hence dust loading was practically invariant over the diurnal cycle. This possibly suggests unchanging conditions in the boundary layer thermal structure and in the concentration and altitude of the dust.

5.4. Model Validation

[32] Next, to validate model performance, computed surface irradiances ($\downarrow$) are compared with downwelling broadband measurements from a collocated PIR. Figure 8a shows the resulting modeled (blue markers) and observed (red markers) irradiances. Overall, both data sets (measurements versus model) correlate reasonably well (linear correlation coefficient of ~0.93) with a mean absolute difference of around -4.4 ± 13.6 Wm^{-2} (1-σ standard deviation). Although the variability is large, the majority of points (~78%) are still within the total combined uncertainty of 15 Wm^{-2}. Apparent are two distinct periods; one which extends from 19 April–27 April and is more characteristic of background dust and the second (1–6 May) which represents heavier dust conditions. The model closely tracks the PIR during period 1 which includes those days (22–24 April) having very low water vapor amounts (RH ~10–15%) and a minimal dust AOT of $\tau = 0.2$ (Figure 7a). The corresponding irradiances (~200 Wm^{-2}) are the smallest values recorded during the deployment. A steady increase in dust loading near the end of period 1, leads to larger downward emissions of ~300 Wm^{-2} for a net gain in LW energy at the surface of nearly 100 Wm^{-2}. For period 2 during the more active dust phase, the data sets do not track as well as the first which is likely due to a much larger uncertainty in the actual dust physicochemical properties (e.g., particle composition) and changing atmospheric conditions. Misclassified dust scenes which likely contain complex dust-cloud mixtures as observed by total sky imager (TSI) data and MPL profiles, may also have contributed to the observed offsets. The resulting scatterplot, color-coded according to AOT, is presented in Figure 8b. 78% of the correlating data points have differences <15 Wm^{-2} as indicated by the dotted black lines. Linear regression coefficients are 0.70 and 74.9 for the slope and offset, respectively, where the large offset is indicative of model uncertainties, particularly water vapor and potential cloud biases. The effect of water vapor was tested by reducing the model's total column water vapor amount for the dry period of 22–24 April which led to a decrease of 45 Wm^{-2} in the offset. Further, by excluding the PIR's larger irradiance values (circled region), which by inspecting TSI data were found to be more influenced by cloud than by dust, yielded a slope and offset of 0.96 and 4.4, respectively.

5.5. Surface DRE$_{LW}$
5.5.1. Instantaneous Values

[33] The resulting time series of surface instantaneous DRE$_{LW}$ is presented in Figure 8c where DRE$_{LW}$ conservatively ranges from ~2.3–20 Wm^{-2} for 95% of the points but can reach as high as 28 Wm^{-2} however; this may be attributed to complex dust-cloud mixtures where cloud effects dominate. The upper end of the range in DRE$_{LW}$ found in this study is comparable to the LW values (~19.92–26.36 Wm^{-2}) reported by *Huang et al.* [2009] in their study over the Taklamakan Desert during July 2006 ($0.4 \leq \tau \leq 0.9$). Note their higher values reflect being directly over the source region. Further, the maximum LW values from the current study are about a factor of two larger than those found at Cape Verde (2–10 Wm^{-2}). The mean (+1-σ
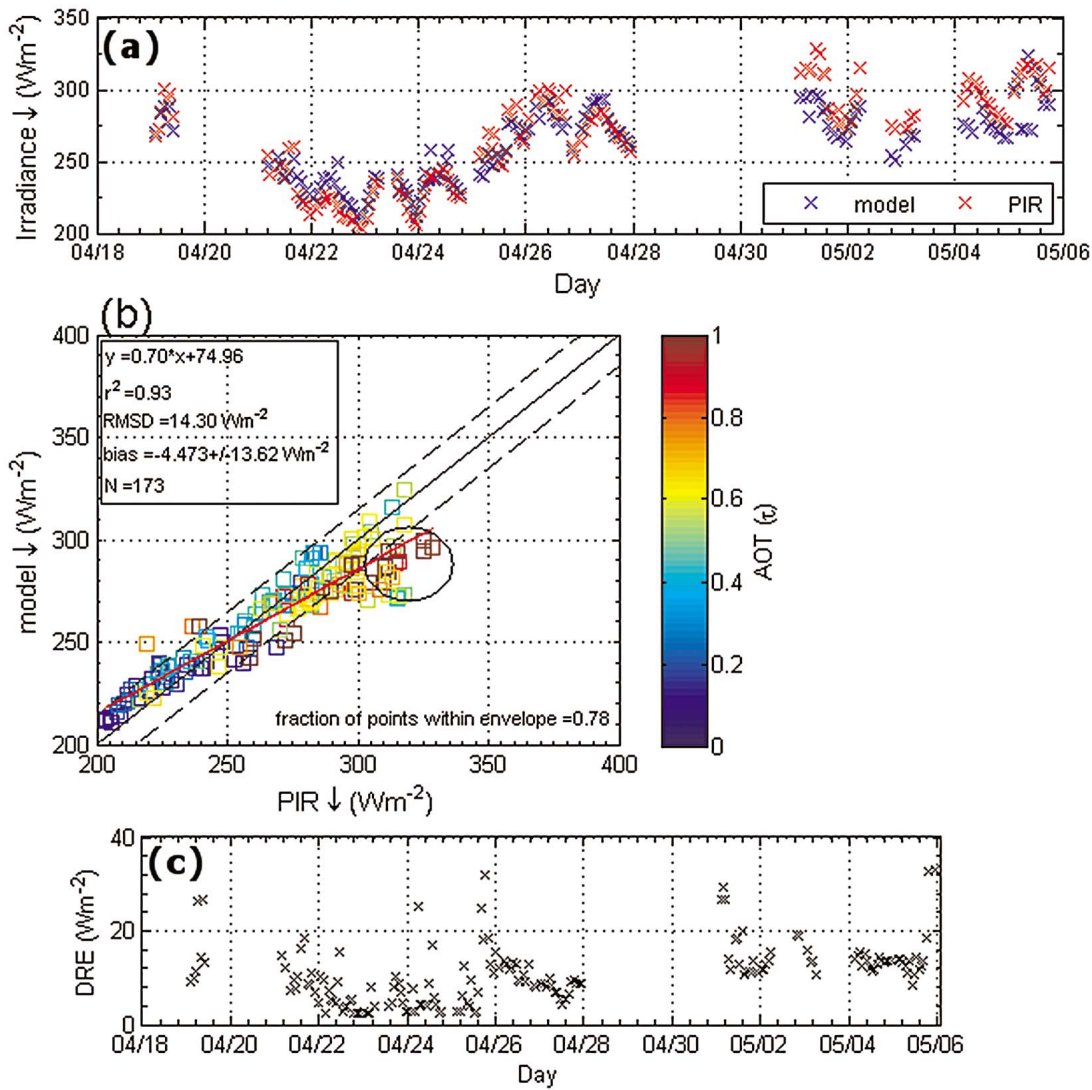
Figure 8. (a) Downwelling surface irradiances from both measurements (PIR, red markers) and model simulations (blue markers) over study period. Model irradiances track well with the PIR with a linear correlation coefficient of 93%. (b) Scatterplot of PIR versus model color-coded according to AOT. Black central line is the 1:1 line; black outer lines (dotted) represent area bounded by estimated uncertainty (measurements + model) of ±15 Wm^{-2}, and red line is the linear best fit. (c) Time series of instantaneous DRE$_{LW}$. See text for further details.

standard deviation) instantaneous DRE$_{LW}$ for the study period is 14.3 ± 9.7 Wm^{-2} and becomes 10.1 ± 4.9 Wm^{-2} if the high values (>20 Wm^{-2}) are excluded. This compares to a mean value of 6.4 Wm^{-2} at Cape Verde. The mean daytime and nighttime values are comparable at around 12.0 Wm^{-2}, again suggesting the dust loading and/or boundary layer thermal structure are relatively invariant over the diurnal cycle. DRE$_{LW}$ for 'background dust' (19–27 April) and 'heavy dust' (1–6 May) were found to be about 10 ± 7 Wm^{-2} and 18 ± 8 Wm^{-2}, respectively, with the latter period being almost 2 times larger than the first. Relative to the observed and modeled ranges in surface DRE$_{LW}$ for clouds (∼30–80 Wm^{-2} [e.g., *Lockwood*, 1992; *Heidinger and Cox*, 1996]) and greenhouse gases (∼2 Wm^{-2} [e.g., *Philipona et al.*, 2004]), this study's upper range in DRE$_{LW}$ represents a significant perturbation to the climate system

which has important implications for better understanding regional changes in both surface temperatures and moisture budgets. For example, the large DRE$_{LW}$ from dust could conceivably explain, in part, observed decreases in diurnal temperature range trends in China as reported by *Zhou et al.* [2009].

5.5.2. Forcing Efficiency

[34] The relationship of instantaneous DRE$_{LW}$ with AOT is illustrated in Figure 9a (top curve – 'x' symbols) where high points likely associated with mixed dust-cloud systems are excluded. The results from Cape Verde during the NAMMA field study are also given (lower curve – 'o' symbols) for comparing DRE$_{LW}$ at two distinct surface sites. The LW forcing efficiency at Cape Verde was found to be about 16 Wm$^{-2}\tau^{-1}$ ($0.2 \leq \tau \leq 0.65$). For direct comparison, a linear fit to the Zhangye data yields a LW forcing

$$y = 35 \cdot x + 1.3$$
$$y = -8.1 \cdot x^2 + 41 \cdot x + 0.66$$
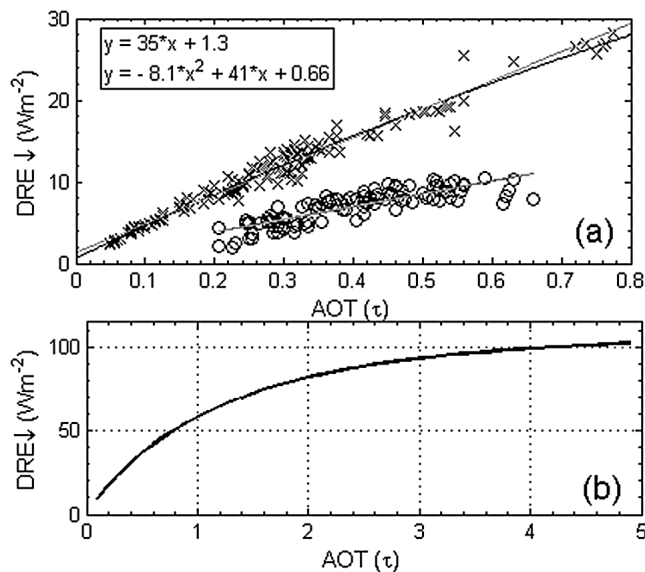
Figure 9. (a) Instantaneous DRE_{LW} at Zhangye (two top curves) and Cape Verde (bottom curve) as functions of AOT. Shown are the corresponding fits to the data. The linear and nonlinear equations shown pertain to the uppermost gray and black curves, respectively for this study. (b) Model simulation illustrating DRE_{LW} reaching steady state conditions for large AOT. See text for details.

efficiency of about 35 $Wm^{-2}\tau^{-1}$, over a factor of two higher than at Cape Verde, similar to the instantaneous values [*Hansell et al.*, 2010]. This is likely due to Zhangye's close proximity to the source region (Figure 1), where larger particles interact more efficiently with LW radiation [*Yoshioka et al.*, 2007], and differences in the absorbing properties of the local dust aerosol (section 5.1). This can also be attributed to differences in the surface properties (land versus ocean) where hotter desert surfaces emit more LW energy and environmental conditions (desert versus maritime) such as in the humidity and temperature profiles between the two test sites. The LW forcing efficiency in this study is similar to that reported by *Xia and Zong* [2009] who, using satellite data, reported an annual range of 18.3–39.3 $Wm^{-2}\tau^{-1}$ in the LW forcing efficiency of dust over the Taklamakan Desert ($0.51 \leq \tau \leq 0.62$). Interestingly at the visible wavelengths ($\lambda = 0.55$ μm), *Ge et al.* [2010] reported a larger forcing efficiency ($\sim$40 $Wm^{-2}\tau^{-1}$ greater) at Zhangye compared to that found in Niamey, Africa [*McFarlane et al.*, 2009] during the 2006 spring season. If the points associated with mixed dust-cloud systems are retained, the forcing efficiency is reduced by $\sim$1 $Wm^{-2}\tau^{-1}$ or 34 $Wm^{-2}\tau^{-1}$ due to nonlinear effects at higher AOT.

[35] Model calculations show that DRE_{LW} eventually saturates (i.e., DRE_{LW} is constant with AOT) at some critical AOT value. For demonstration purposes, arbitrary model inputs are used to illustrate this behavior under high dust loading conditions (Figure 9b) where perturbations in the surface energetics eventually reach a steady state value. This effect can also be observed in the heating rate profiles (not shown) where beyond a critical AOT, the derivative (dT/dt) approaches zero and layer temperatures are nearly constant. To assess the nonlinear effect, a quadratic fit to the data was

also applied (Figure 9a) which yields a forcing efficiency of about 32.9 $Wm^{-2}\tau^{-1}$. Similar fits about the mean (not shown to preserve clarity) using minimum and maximum size distributions yield a range in forcing efficiency of about 31–34 $Wm^{-2}\tau^{-1}$ ($0 \leq \tau \leq 0.83$) and can be as high as 35 $Wm^{-2}\tau^{-1}$ depending on the type of fit applied. Besides particle size, this range also accounts for uncertainties in atmospheric temperatures and water vapor in the boundary layer using the same perturbations shown in Table 2.

5.5.3. LW Significance

[36] Last, we address the LW significance of DRE at the surface relative to that in the SW. Following *Liu et al.* [2003], the diurnally averaged DRE_{SW} forcing efficiency is defined as

$$DRE_{SW} = \frac{1}{24} \int_{sunrise}^{sunset} IDRE_{SW}(H)dH \qquad (2)$$

where $IDRE_{SW}$ is the instantaneous DRE_{SW} calculated from the model at local time H. Note that SW DRE is also defined with respect to downward irradiance similar to DRE_{LW}. For this study, the diurnally averaged DRE_{SW} forcing efficiency was found to be around -60 $Wm^{-2}\tau^{-1}$ (Figure 10). This value is on the lower end of the range (-55 to -106 $Wm^{-2}\tau^{-1}$) computed by *Kim et al.* [2005] for Asian dust but differs from the average value of -95.1 $Wm^{-2}\tau^{-1}$ at Zhangye reported by *Ge et al.* [2010]. This disparity can likely be explained by differences in the methodologies and in the resulting SW optical properties between dust models. As pointed out in section 5.1, the SW differences in optical properties can potentially be explained by lack of strong absorbers such as hematite or soot in this study's model. If the model dust absorption is perturbed +15%, for example, the DRE_{SW} forcing efficiency increases by -13 $Wm^{-2}\tau^{-1}$ yielding a total DRE_{SW} of -73 $Wm^{-2}\tau^{-1}$. Hence greater particle absorption will lead to larger forcing efficiencies. The computed range in DRE_{LW} (31–35 $Wm^{-2}\tau^{-1}$) amounts to an estimated LW significance of 51–58% relative to the SW which is at least 9% higher than that found at Cape Verde during the NAMMA-2006 study on Saharan dust. In other words, about one-half of the SW cooling by dust is compensated by its LW warming effects, much larger than the one-third compensation reported in *Huang et al.* [2009] using CALIPSO observations over the Taklamakan Desert. The main difference is that the latter study used a much smaller

$$y = -60 \cdot x + 1.9$$
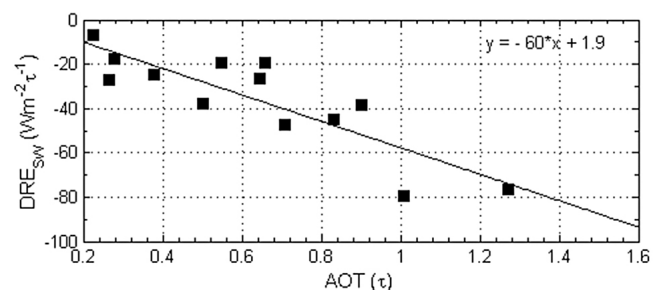
Figure 10. Diurnally averaged DRE_{SW} forcing efficiency over study period at Zhangye used to assess the LW significance. See text for details.

Table 3. Surface DRE$_{LW}$ Results Summary

Parameter	This Study (Wm^{-2})	Comparisons (Wm^{-2})	Comments[a]
Range in DRE$_{LW}$	2.3–20[b]	Cape Verde: 2–10[c]; Taklamakan: ~19–26[d]	OS/G/Sept, LS/S/July
Mean DRE$_{LW}$ (total)	10.1 ± 4.9[e]	Cape Verde: 6.4	OS/G/Sept
Mean DRE$_{LW}$ (background)[f]	10 ± 7	–	–
Mean DRE$_{LW}$ (heavy)[f]	18 ± 8	–	–
Forcing efficiency	31–35 Wm$^{-2}\tau^{-1}$	Cape Verde: 16 Wm$^{-2}\tau^{-1}$; Taklamakan: 18.3–39.3 Wm$^{-2}\tau^{-1g}$	OS/G/Sept, LS/S/May[g]

[a]OS = ocean surface; LS = land surface; G = ground-based instruments; S = satellite. The month refers to study period.
[b]Can be as high as 28 Wm^{-2}.
[c]*Hansell et al.* [2010].
[d]*Huang et al.* [2009]: 7/24, 7/26, and 7/29–7/31 2006.
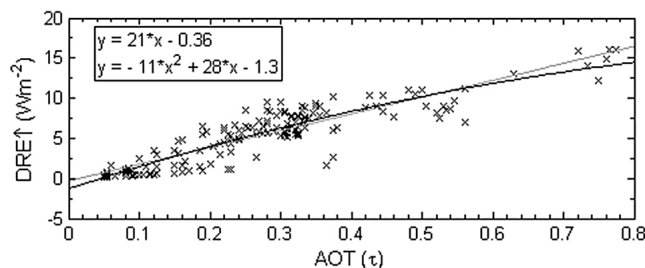[e]Can be as high as 14.3 ± 9.7 Wm^{-2}.
[f]Background dust (19–27 April); heavy dust (1–6 May).
[g]*Xia and Zong* [2009]; study focuses on May from 2001 to 2006.

SSA which led to a much larger SW surface forcing [*Huang et al.*, 2007]. *Xia and Zong* [2009], on the other hand, using satellite observations (MISR and CERES) also over the Taklamakan Desert, reported that the LW warming effect can offset 58% of the SW cooling, similar to this study. Compared to *Huang et al.* [2009], the larger LW significance in the latter work is because of a smaller SW surface forcing. The key surface DRE$_{LW}$ results presented in section 5.5 and their comparisons are summarized in Table 3. Differences between observing platform (ground-based instruments versus satellite), surface type (ocean versus land), and time of year of each study are indicated in the last column.

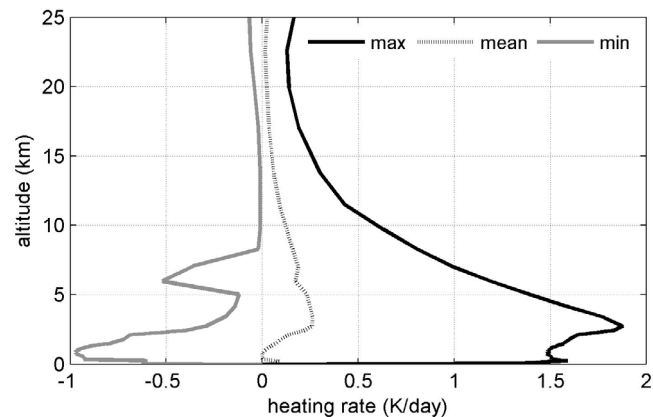### 5.6. TOA DRE$_{LW}$ and Heating Rates

[37] Employing the same model parameters used to calculate surface DRE$_{LW}$, the instantaneous DRE$_{LW}$ of outgoing LW radiation (OLR) at the TOA are determined. Figure 11 shows the instantaneous values plotted against AOT with a correlation coefficient of ~0.90 and having an average (1-σ standard deviation) of 5.2 ± 3.7 Wm^{-2} and a range of 0.18–16.1 Wm^{-2}. Due to the much higher dust layers, *Huang et al.* [2009] using CALIPSO observations, reported larger values at the TOA (28.64–33.65 Wm^{-2}). Similar to the surface, DRE$_{LW}$ at the TOA shows a near linear dependence for optically thinner media but begins to display nonlinear effects at higher optical depths. DRE$_{LW}$ forcing efficiencies at the TOA were found to be in the range of 17–21 Wm$^{-2}\tau^{-1}$ where the LW irradiance enhancement at the surface is seen as a reduction in OLR due to absorption

in the intervening dust layers. Hence, the sign of DRE$_{LW}$ at the TOA is negative (i.e., cooling). For the current study, a larger reduction in OLR was found exceeding that identified during the NAMMA study by up to 60%.

[38] Perturbations in heating rates (LW + SW) due to the presence of dust are calculated by differencing the all-sky (clear-sky + dust) and clear-sky heating rates for the model layers. As before, the model's dust vertical distribution was based on an AOT scale height of 3 km, roughly corresponding to that observed by the MPL. Figure 12 shows the minimum, mean, and maximum heating rate profiles for the study period over the column atmosphere up through 25 km. Low level heating in the boundary layer due to strong dust absorption varied from near zero and reached peaks of about 1.5 and 1.75 K/day at the surface and an altitude of ~2.5 km, respectively. On average the heating rates exhibited values near 0.25 K/day with areas of negative heating associated with radiative cooling of both surface and elevated dust layers, including a smaller secondary peak of cooling at an altitude of around 6 km. *Huang et al.* [2009], using CALIPSO derived vertical distributions of dust

Figure 11. Instantaneous TOA DRE$_{LW}$ at Zhangye over study period as a function of AOT. Shown are the corresponding fits to the data. See text for details.

Figure 12. Minimum, maximum, and mean dust heating rate (LW+SW) profiles during study period. On average the heating rates were ~0.25 K/day peaking at an altitude of around 3–4 km with the largest heating rates reaching nearly 2 K/day. The minimum profile shows regions of radiative cooling at layers near the surface and about 6 km. See text for details.

extinction for cases in July 2006, reported heating rates that varied between 1 and 3 K/day depending on dust load, with maximum heating reaching 5.5 K/day. Again the larger values are not surprising since this study was focused directly over the desert source. Strong peaks in the heating profiles demonstrate the potential for dust to impact surface temperatures and atmospheric stability.

6. Summary

[39] The DRE of dust aerosol around the desert regions of northwestern China have been a major focus of recent works. Although there are many SW studies of dust DRE for this region, the LW effects, particularly those derived using surface measurements, are not as abundant. In this work, we use ground-based sensors in Zhangye during AMY08 to examine DRE_{LW} over a 2-week dust-intense period to help advance our understanding of the LW energetics of Asian dust. A regional dust optical model was constructed by combining previously measured soil mineralogy data at Zhangye with particle microphysical measurements from this deployment. Employing a broadband RTM constrained by temporally resolved AERI retrieved LW AOTs and atmospheric state parameters along with surface measured irradiances, surface instantaneous DRE_{LW} were found to vary conservatively between 2.3 and 20 Wm^{-2}, but reached as high as 28 Wm^{-2}. The upper end of this range is comparable to observed and modeled cloud DRE_{LW} ($\sim$30–80 Wm^{-2}) and exceeds that due to greenhouse gases ($\sim$2 Wm^{-2}); hence the results presented represent a significant perturbation to the climate system. A conservative estimate of the mean surface instantaneous DRE_{LW} (+1-σ standard deviation) for the period was found to be 10.1 $\pm$ 4.9 Wm^{-2} but can be as large as 14.3 $\pm$ 9.7 Wm^{-2}. It was also found that both daytime and nighttime DRE_{LW} are approximately equal with mean values of $\sim$12.0 Wm^{-2} suggesting the dust loading and/or boundary layer thermal structure are relatively invariant over the diurnal cycle. This differs from the larger nighttime effects observed over Cape Verde during the NAMMA-2006 study of Saharan dust, where the effective emission temperatures of dust were more likely influenced during the nighttime.

[40] Accounting for uncertainties in aerosol properties and atmospheric state, and considering the fit to the data, the DRE_{LW} forcing efficiency (per unit AOT) can range from 31 to 35 $Wm^{-2}\tau^{-1}$ which is about a factor of two higher than what was found at Cape Verde. This is most likely attributed Zhangye's close proximity to the major desert sources and the larger LW dust absorption ($\sim$50% larger) which inevitably leads to increased downwelling surface emissions. Previous findings of reported SW differences between Asian and African dust lend support to these results. Comparing the LW contributions of DRE at the surface to that in the SW reveals that about one-half of the SW cooling by dust is compensated by its LW warming effects, at least 9% larger than what was found over Cape Verde. Previous studies over the Taklamakan Desert reveal that about one-third to one-half of the LW warming offsets SW cooling, comparable to the current work. A larger reduction in OLR was found exceeding that identified during the NAMMA study by up to 60%. Boundary layer heating on average was about

0.25 K/day but reached as high as 1.5–1.75 K/day which peaked between the surface and at an altitude of $\sim$2.5 km coinciding with MPL dust observations.

[41] Compared to maritime ocean sites, this study illustrates the significance of the LW radiative effects of dust aerosols over desert land sites where hotter surfaces emit more LW energy which can interact more readily with larger sized particles near the source region. The pronounced radiative effects are mainly attributed to the following key elements: (1) Zhangye's proximity to the major deserts in northwestern China, (2) larger absorbing properties of the regional dust aerosols, (3) an elevated land surface ($\Delta h \approx 1.5$ km ASL), and (4) dry desert conditions where the water vapor path is small.

[42] The LW radiative effect of dust at Zhangye likely plays an important role in the regional changes of surface temperatures and moisture budgets, and is therefore a crucial parameter for understanding the region's atmospheric stability and ensuing surface-atmosphere exchange processes.

References

Aronson, J. R., and P. F. Strong (1975), Optical constants of minerals and rocks, *Appl. Opt.*, *14*, 2914–2920.

Aumann, H. H., et al. (2003), AIRS/AMSU/HSB on the Aqua Mission: Design, science objectives, data products, and processing systems, *IEEE Trans. Geosci. Remote Sens.*, *41*, 253–264.

Chaudhry, Z., J. Vanderlei Martins, Z. Li, S. C. Tsay, H. Chen, T. Wang, T. Wen, C. Li, and R. R. Dickerson (2007), In situ measurements of aerosol mass concentration and radiative properties in Xianghe, SE of Beijing, *J. Geophys. Res.*, *112*, D23S90, doi:10.1029/2007JD009055.

Drummond, D. G. (1935), The infra-red absorption spectra of quartz and fused silica from 1 to 7.5 microns, *Proc. R. Soc. London, Ser. A*, *153*, 328–339, doi:10.1098/rspa.1936.0005.

Egan, W. G., and T. W. Hilgeman (1979), *Optical Properties of Inhomogeneous Materials: Applications to Geology, Astronomy, Chemistry, and Engineering*, Academic, New York.

Feltz, W. F., W. L. Smith, H. B. Howell, R. O. Knuteson, H. Woolf, and H. E. Revercomb (2003), Near-continuous profiling of temperature, moisture, and atmospheric stability using the Atmospheric Emitted Radiance Interferometer (AERI), *J. Appl. Meteorol.*, *42*, 584–597, doi:10.1175/1520-0450(2003)042<0584:NPOTMA>2.0.CO;2.

Fu, Q., and K. N. Liou (1992), On the correlated K-distribution method for radiative transfer in nonhomogeneous atmospheres, *J. Atmos. Sci.*, *49*, 2139–2156, doi:10.1175/1520-0469(1992)049<2139:OTCDMF>2.0.CO;2.

Fu, Q., and K. N. Liou (1993), Parameterization of the radiative properties of cirrus clouds, *J. Atmos. Sci.*, *50*, 2008–2025, doi:10.1175/1520-0469(1993)050<2008:POTRPO>2.0.CO;2.

Fu, Q., T. J. Thorson, J. Su, J. M. Ge, and J. P. Huang (2009), Test of Mie-based single-scattering properties of non-spherical dust aerosols in radiative flux calculations, *J. Quant. Spectrosc. Radiat. Transfer*, *110*, 1640–1653, doi:10.1016/j.jqsrt.2009.03.010.

Ge, J. M., J. Su, T. P. Ackerman, Q. Fu, J. P. Huang, and J. S. Shi (2010), Dust aerosol optical properties retrieval and radiative forcing over northwestern China during the 2008 China-U.S. joint field experiment, *J. Geophys. Res.*, *115*, D00K12, doi:10.1029/2009JD013263.

Gray, E. D. (Ed.) (1963), *American Institute of Physics Handbook*, 2nd ed., McGraw-Hill, New York.

Hansell, R. A., S. C. Ou, K. N. Liou, J. K. Roskovensky, S. C. Tsay, C. Hsu, and Q. Ji (2007), Simultaneous detection/separation of mineral dust and cirrus clouds using MODIS thermal infrared window data, *Geophys. Res. Lett.*, *34*, L11808, doi:10.1029/2007GL029388.

Hansell, R. A., K. N. Liou, S. C. Ou, S. C. Tsay, Q. Ji, and J. S. Reid (2008), Remote sensing of mineral dust aerosol using AERI during the UAE2: A modeling and sensitivity study, *J. Geophys. Res.*, *113*, D18202, doi:10.1029/2008JD010246.

Hansell, R. A., S. C. Tsay, Q. Ji, N. C. Hsu, M. J. Jeong, S. H. Wang, J. S. Reid, K. N. Liou, and S. C. Ou (2010), An assessment of the surface longwave direct radiative effect of airborne Saharan dust during the NAMMA field campaign, *J. Atmos. Sci.*, *67*, 1048–1065, doi:10.1175/2009JAS3257.1.

Hansell, R. A., J. S. Reid, S. C. Tsay, T. L. Roush, and O. V. Kalashnikova (2011), A sensitivity study on the effects of particle chemistry, asphericity and size on the mass extinction efficiency of mineral dust in the Earth's atmosphere: From the near to thermal IR, *Atmos. Chem. Phys.*, *11*, 1527–1547, doi:10.5194/acp-11-1527-2011.

Haywood, J. M., R. P. Allan, I. Culverwell, T. Slingo, J. Edwards, and N. Clerbaux (2005), Can desert dust explain the outgoing longwave radiation anomaly over the Sahara during July 2003?, *J. Geophys. Res.*, *110*, D05105, doi:10.1029/2004JD005232.

Heidinger, A. K., and S. K. Cox (1996), Finite cloud effects in longwave radiative transfer, *J. Atmos. Sci.*, *53*, 953–963, doi:10.1175/1520-0469(1996)053<0953:FCEILR>2.0.CO;2.

Highwood, E. J., J. M. Haywood, M. D. Silverstone, S. M. Newman, and J. P. Taylor (2003), Radiative properties and direct effect of Saharan dust measured by the C-130 aircraft during Saharan Dust Experiment (SHADE): 2. Terrestrial spectrum, *J. Geophys. Res.*, *108*(D18), 8578, doi:10.1029/2002JD002552.

Holben, H. B., et al. (1998), AERONET—A federated instrument network and data archive for aerosol characterization, *Remote Sens. Environ.*, *66*, 1–16, doi:10.1016/S0034-4257(98)00031-5.

Hsu, N. C., J. R. Herman, and C. Weaver (2000), Determination of radiative forcing of Saharan dust using combined TOMS and ERBE data, *J. Geophys. Res.*, *105*(D16), 20,649–20,661, doi:10.1029/2000JD900150.

Huang, J., P. Minnis, Y. Yi, Q. Tang, X. Wang, Y. Hu, Z. Liu, K. Ayers, C. Trepte, and D. Winker (2007), Summer dust aerosols detected from CALIPSO over the Tibetan Plateau, *Geophys. Res. Lett.*, *34*, L18805, doi:10.1029/2007GL029938.

Huang, J., Q. Fu, J. Su, Q. Tang, P. Minnis, Y. Hu, Y. Yi, and Q. Zhao (2009), Taklimakan dust aerosol radiative heating derived from CALIPSO observations using the Fu-Liou radiation model with CERES constraints, *Atmos. Chem. Phys.*, *9*, 4011–4021, doi:10.5194/acp-9-4011-2009.

Jeong, G. Y. (2008), Bulk and single-particle mineralogy of Asian dust and a comparison with its source soils, *J. Geophys. Res.*, *113*, D02208, doi:10.1029/2007JD008606.

Kim, D.-H., B. J. Sohn, T. Nakajima, T. Takamura, T. Takemura, B. C. Choi, and S. C. Yoon (2004), Aerosol optical properties over East Asia determined from ground-based sky radiation measurements, *J. Geophys. Res.*, *109*, D02209, doi:10.1029/2003JD003387.

Kim, D. H., B. J. Sohn, T. Nakajima, and T. Takamura (2005), Aerosol radiative forcing over East Asia determined from ground-based solar radiation measurements, *J. Geophys. Res.*, *110*, D10S22, doi:10.1029/2004JD004678.

Lau, K.-M., M. K. Kim, and K. M. Kim (2006), Asian summer monsoon anomalies induced by aerosol direct forcing: The role of the Tibetan Plateau, *Clim. Dyn.*, *26*, 855–864, doi:10.1007/s00382-006-0114-z.

Lau, K.-M., et al. (2008), The Joint Aerosol-Monsoon Experiment: A new challenge for monsoon climate research, *Bull. Am. Meteorol. Soc.*, *89*, 369–383, doi:10.1175/BAMS-89-3-369.

Li, C., L. T. Marufu, R. R. Dickerson, Z. Li, T. Wen, Y. Wang, P. Wang, H. Chen, and J. W. Stehr (2007), In-situ measurements of trace gases and aerosol optical properties at a rural site in northern China during East Asian Study of Tropospheric Aerosols: An International Regional Experiment 2005, *J. Geophys. Res.*, *112*, D22S04, doi:10.1029/2006JD007592.

Li, C., et al. (2010), Anthropogenic air pollution observed near dust source regions in northwestern China during springtime 2008, *J. Geophys. Res.*, *115*, D00K22, doi:10.1029/2009JD013659.

Li, Z., K.-H. Lee, Y. Wang, J. Xin, and W.-M. Hao (2010), First observational-based estimates of cloud-free aerosol radiative forcing across China, *J. Geophys. Res.*, *115*, D00K18, doi:10.1029/2009JD013306.

Li, Z., et al. (2011), East Asian Studies of Tropospheric Aerosols and their Impact on Regional Climate (EAST-AIRC): An overview, *J. Geophys. Res.*, *116*, D00K34, doi:10.1029/2010JD015257.

Liu, J., Y. Zheng, Z. Li, and R. Wu (2008), Ground-based remote sensing of aerosol optical properties in one city in northwest China, *Atmos. Res.*, *89*, 194–205, doi:10.1016/j.atmosres.2008.01.010.

Liu, X., J. Wang, and S. Christopher (2003), Shortwave direct radiative forcing of Saharan dust aerosols over the Atlantic Ocean, *Int. J. Remote Sens.*, *24*, 5147–5160, doi:10.1080/0143116031000114824.

Lockwood, J. G. (1992), Impact of cloud longwave radiative surface forcing on inception loss from a coniferous forest canopy, *Q. J. R. Meteorol. Soc.*, *118*, 1235–1239, doi:10.1002/qj.49711850811.

Long, L. L., M. R. Querry, R. J. Bell, and R. W. Alexander (1993), Optical properties of calcite and gypsum in crystalline and powdered form in the infrared and far-infrared, *Infrared Phys.*, *34*(2), 191–201.

Longtin, D. R. (1988), A wind dependent desert aerosol model: Radiative properties, *Rep. AFL-TR-88-0122*, Air Force Geophys. Lab., Hanscom Air Force Base, Mass.

Marra, A. C., R. Politi, A. Blanco, R. Brunetto, S. Fonti, G. A. Marzo, and V. Orofino (2006), Optical constants of particulate minerals from reflectance measurements: The case of calcite, *J. Quant. Spectrosc. Radiat. Transfer*, *100*, 250–255, doi:10.1016/j.jqsrt.2005.11.042.

McClatchley, R. A., R. W. Fenn, J. E. A. Selby, F. E. Volz, and J. S. Garing (1972), Optical properties of the atmosphere, *Environ. Res. Pap.*, *411*, 107 pp., Air Force Cambridge Res. Lab., Cambridge, Mass.

McFarlane, S. A., E. I. Kassianov, J. Barnard, C. Flynn, and T. P. Ackerman (2009), Surface shortwave aerosol radiative forcing during the Atmospheric Radiation Measurement Mobile Facility deployment in Niamey, Niger, *J. Geophys. Res.*, *114*, D00E06, doi:10.1029/2008JD010491.

Menon, S., J. Hansen, L. Nazarenko, and Y. Luo (2002), Climate effects of black carbon aerosols in China and India, *Science*, *297*, 2250–2253, doi:10.1126/science.1075159.

Mishchenko, M. I., A. A. Lacis, B. E. Carlson, and L. D. Travis (1995), Nonsphericity of dust-like tropospheric aerosols: Implications for aerosol remote sensing and climate modeling, *Geophys. Res. Lett.*, *22*, 1077–1080, doi:10.1029/95GL00798.

Mooney, T., and R. F. Knacke (1985), Optical constants of chlorite and serpentine between 2.5 and 50 μm, *Icarus*, *64*, 493–502, doi:10.1016/0019-1035(85)90070-3.

Nousiainen, T. (2009), Optical modeling of mineral dust particles: A review, *J. Quant. Spectrosc. Radiat. Transfer*, *110*, 1261–1279, doi:10.1016/j.jqsrt.2009.03.002.

Nurhayati, N., and T. Nakajima (2012), A study of optical properties at the global GAW station Bukit Kototabang, Sumatra, Indonesia, *Atmos. Environ.*, *46*, 597–606, doi:10.1016/j.atmosenv.2010.10.057.

Ossenkopf, V. (1991), Effective-medium theories for cosmic dust grains, *Astron. Astrophys.*, *251*, 210–219.

Péré, J.-C., V. Pont, M. Mallet, and B. Bessagnet (2009), Mapping of PM10 surface concentrations derived from satellite observations of aerosol optical thickness over south eastern France, *Atmos. Res.*, *91*, 1–8, doi:10.1016/j.atmosres.2008.05.001.

Philipona, R., B. Durr, C. Marty, A. Ohmura, and M. Wild (2004), Radiative forcing - measured at Earth's surface - corroborate the increasing greenhouse effect, *Geophys. Res. Lett.*, *31*, L03202, doi:10.1029/2003GL018765.

Philipp, H. R. (1985), *Silicon Dioxide (SiO₂), Type α (Crystalline) in Handbook of Optical Constants of Solids*, edited by E. D. Palik, 719 pp., Academic, Orlando, Fla.

Pollack, J. B., O. B. Toon, and B. N. Khare (1973), Optical properties of some terrestrial rocks and glasses, *Icarus*, *19*, 372–389, doi:10.1016/0019-1035(73)90115-2.

Rose, F. G., and T. P. Charlock (2002), New Fu-Liou code tested with ARM Raman lidar and CERES in pre-CALIPSO exercise, paper presented at 11th Conference on Atmospheric Radiation, Am. Meteorol. Soc., Ogden, Utah, 3–7 June.

Roush, T. L. (2010), Estimated optical constants of calcite, paper presented at 2010 Fall Meeting, AGU, San Francisco, 13–17 Dec.

Roush, T. L., F. Esposito, G. R. Rossman, and L. Colangeli (2007), Estimated optical constants of gypsum in the regions of weak absorptions: Application of scattering theories and comparisons to independent measurements, *J. Geophys. Res.*, *112*, E10003, doi:10.1029/2007JE002920.

Seemann, S. W., E. E. Borbas, R. O. Knuteson, G. R. Stephenson, and H.-L. Huang (2008), Development of a global infrared land surface emissivity database for application to clear sky sounding retrievals from multi-spectral satellite radiance measurements, *J. Appl. Meteorol. Climatol.*, *47*, 108–123, doi:10.1175/2007JAMC1590.1.

Shettle, E. P., and R. W. Fenn (1979), Models for the aerosols for the lower atmosphere and the effects of humidity variations on their optical properties, *Environ. Res. Pap., AFGL-TR-79-0214*, Air Force Geophys. Res. Lab., Hanscom Air Force Base, Mass.

Spitzer, W. G., and D. A. Kleinman (1961), Infrared lattice bands of quartz, *Phys. Rev.*, *121*, 1324–1335, doi:10.1103/PhysRev.121.1324.

Thomas, M., and C. Gautier (2009), Investigations of the March 2006 African dust storm using ground-based column-integrated high spectral resolution infrared (8–13 mm) and visible aerosol optical thickness

measurements: 2. Mineral aerosol mixture analyses, *J. Geophys. Res.*, *114*, D14209, doi:10.1029/2008JD010931.

Tsay, S.-C. (2009), Outbreaks of Asian dust storms: An overview from satellite and surface perspectives, in *Recent Progress in Atmospheric Sciences: Applications to the Asia Pacific Region*, edited by K. N. Liou and M. D. Chou, pp. 373–401, World Sci., Singapore.

Volz, F. E. (1973), Infrared optical constants of ammonium sulfate, Sahara dust, volcanic pumice, and flyash, *Appl. Opt.*, *12*, 564–568, doi:10.1364/AO.12.000564.

Wang, X., J. Huang, R. Zhang, B. Chen, and J. Bi (2010), Surface measurements of aerosol properties over northwest China during ARM China 2008 deployment, *J. Geophys. Res.*, *115*, D00K27, doi:10.1029/2009JD013467.

Welton, E. J., J. R. Campbell, J. D. Spinhirne, and V. S. Scott (2001), Global monitoring of clouds and aerosols using a network of micro-pulse lidar systems, *Proc. SPIE Int. Soc. Opt. Eng.*, *4153*, 151–158.

Xia, X., and X. Zong (2009), Shortwave versus longwave direct radiative forcing by Taklimakan dust aerosols, *Geophys. Res. Lett.*, *36*, L07803, doi:10.1029/2009GL037237.

Yoshioka, M., N. M. Mahowald, A. J. Conley, W. D. Collins, D. W. Fillmore, C. S. Zender, and D. B. Coleman (2007), Impact of desert dust radiative forcing on Sahel precipitation: Relative importance of dust compared to sea surface temperature variations, vegetation changes, and greenhouse gas warming, *J. Clim.*, *20*, 1445–1467, doi:10.1175/JCLI4056.1.

Zhang, J., and S. A. Christopher (2003), Longwave radiative forcing of Saharan dust aerosols estimated from MODIS, MISR, and CERES observations on Terra, *Geophys. Res. Lett.*, *30*(23), 2188, doi:10.1029/2003GL018479.

Zhang, X., R. Arimoto, and Z. An (1997), Dust emission from Chinese desert sources linked to variations in atmospheric circulation, *J. Geophys. Res.*, *102*, 28,041–28,047, doi:10.1029/97JD02300.

Zhou, L., A. Dai, Y. Dai, R. S. Vose, C.-Z. Zou, Y. Tian, and H. Chen (2009), Spatial dependence of diurnal temperature range trends on precipitation from 1950 to 2004, *Clim. Dyn.*, *32*, 429–440, doi:10.1007/s00382-008-0387-5.

Zipser, E. J., et al. (2009), The Saharan air layer and the fate of African easterly waves, NASA's AMMA field study of tropical cyclogenesis, *Bull. Am. Meteorol. Soc.*, *90*, 1137–1156, doi:10.1175/2009BAMS2728.1.